Searching for cluster Lego blocks for three-dimensional and two-dimensional assemblies

Qiuying Du,[1] Zhen Wang,[1] Si Zhou,[1,*] Jijun Zhao,[1] and Vijay Kumar[2,3]

[1]*Key Laboratory of Material Modification by Laser, Ion and Electron Beams (Dalian University of Technology), Ministry of Education, Dalian 116024, China*

[2]*Center for Informatics, School of Natural Sciences, Shiv Nadar University, NH-91, Tehsil Dadri, Gautam Buddha Nagar 201314, U. P., India*

[3]*Dr. Vijay Kumar Foundation, 1969 Sector 4, Gurgaon 122001, Haryana, India*

(Received 14 January 2021; accepted 19 May 2021; published 3 June 2021)

Assemblies of clusters have been sought for a long time to synthesize new materials with unprecedented physical phenomena or to integrate desired functionalities for technological applications. However, except for some carbon fullerenes and ligated clusters, little progress has been made in achieving assemblies of other clusters due to their tendency for agglomeration. Here we study interaction in dimers of 34 well-studied endohedrally doped clusters (i.e., superatoms) and propose the criteria for such superatoms to be potential building blocks in terms of surface coordination, charge state, distribution of the highest occupied molecular orbital, and electronic as well as atomic shell (double-shell) closure. From these results, the endohedrally doped Ti@Ge_{16} cage cluster stands out as a suitable building block to assemble solids and nanostructures with outstanding stabilities and diverse physical properties. We report here the finding of antiferromagnetic Mott insulator in metal intercalated two-dimensional crystal of such cluster. Our study provides essential knowledge for achieving stable cluster assemblies of different dimensionalities with precisely tailorable electronic structure for device applications.

DOI: 10.1103/PhysRevMaterials.5.066001

I. INTRODUCTION

The booming research on low-dimensional materials is revolutionizing the manufacture of modern devices and has led to unprecedented performance control at atomic scale. With the discovery of various two-dimensional (2D) materials, van der Waals (vdW) heterostructures with desired properties have been synthesized by stacking different atomic layers together [1]. Recently, this concept of nanoscale Lego blocks has also been realized in one-dimensional (1D) materials by coaxially stacking different kinds of nanotubes [2]. Compared to 1D and 2D structures, clusters have geometric and electronic structures depending on both their size and composition. They constitute a huge family of potential zero-dimensional (0D) Lego blocks and open a larger degree of freedom for assembling new materials [3]. So far, only limited kinds of cluster-based solids have been achieved in the experiment, such as α- and β-boron solids formed by the icosahedron B_{12} units [4], face-centered close-packed C_{60} fullerite [5,6], alkali-metal−Pb solid alloys composed of Pb clusters ($Na_{15}Pb_4$, Na_9Pb_4, Li_7Pb_2, etc.) [7,8], and Zintl compounds made of homoatomic or heteroatomic group 14, 14−14, and 14−15 clusters [9,10].

One critical issue for assembling clusters is the production of identical clusters in macroscopic quantity [11]. Another important prerequisite for clusters being building blocks is to retain their identity after assembling [11], as the large surface area and interaction between clusters usually lead to their agglomeration. In the experiment, great success has been achieved by Tsunoyama *et al.,* who synthesized endohedrally doped Ta@Si_{16} and Ti@Si_{16} cage clusters in bulk quantity of 100 mg that are stabilized by poly(ethylene glycol) dimethyl ether [12]. Bare Ta@Si_{16} clusters deposited on a graphite substrate or C_{60}-terminated surface can have high thermal stability at 700 K and satisfactory oxidation resistance [13]. On the theoretical side, a pioneer study by Khanna and Jena suggested that the stability of a cluster can be substantially enhanced by adjusting its size and/or composition to satisfy the requirement of a closed electronic shell as well as a closed atomic shell (also referred to clusters with doubly closed shells) [11]. Such clusters can be regarded as "superatoms" [14–18] as they usually have large gaps between highest unoccupied molecular orbital (HOMO) and lowest unoccupied molecular orbital (LUMO) and thus are associated with higher chemical stability or inertness [19,20]. This progress has aroused new hope for developing macroscopic cluster-based materials.

In the past two decades, endohedral doping of clusters has emerged as the most effective way to achieve superatoms with high stability. By choosing proper metal dopants following the electron counting rules, it is possible to construct cage clusters with atomic shell closure and simultaneously satisfy the requirement of closed electronic shell with appropriate number of valence electrons [9]. A large inventory of endohedral cage clusters with high symmetry and appreciable HOMO-LUMO gap [9,21–45] has been reported on the basis of different electron counting rules. Among them, some well-studied superatoms are Si@Al_{12} [22] and W@Au_{12} [41,42] icosahedra with highest symmetry (I_h), Ti@Si_{16} Frank-Kasper

*sizhou@dlut.edu.cn

(FK) polyhedron (T_d) [29,32], and Hf@Si_{16} fullerene (D_{4d}) [29,32]. All these clusters have closed electronic shells and sizable HOMO-LUMO gaps. However, in spite of having doubly closed shells, many of them exhibit significant interaction between each other [29,46–52]. Therefore, it remains difficult to achieve stable clusters as Lego blocks for assembling vdW-type solids similar to the 1D and 2D counterparts mentioned above. The key to overcome this challenge is to understand the origin of the desired inertness of clusters and illuminate the complete criteria for screening weakly interacting clusters.

To this end, herein we consider 34 superatoms as potential building blocks for cluster assemblies and examine interaction between their dimers. These results are used to extract the criteria for clusters to serve as 0D Lego blocks in terms of the geometric features, charge, as well as HOMO distribution of these candidate clusters. Following these criteria, suitable building blocks for cluster assemblies have been screened. The stabilities and electronic band structures of various 2D and 3D cluster-assembled structures are then explored, demonstrating the feasibility and rich physical properties of these innovative materials for device applications.

II. COMPUTATIONAL DETAILS

All *ab initio* calculations were performed with the VASP code [53], using plane-wave basis set with energy cutoff of 400 eV, projector augmented wave potentials [54], and Perdew, Burke, and Ernzerhof (PBE) exchange-correlation functional [55] with Grimme's semiempirical D3 dispersion correction (PBE-D3) [56]. Atomic structures were fully optimized under the convergence criteria of 10^{-8} eV for the energy and 10^{-4} eV/Å for the force on each ion, respectively. Each cluster monomer or dimer was placed in a cubic supercell with a large dimension of 25 Å, and only the Γ point was used to sample the Brillouin zone. For each cluster dimer, we considered many possible orientations and magnetic couplings and calculated the dimerization energy (E_d) defined as

$$E_d = E_{\text{monomer}1} + E_{\text{monomer}2} - E_{\text{dimer}}, \quad (1)$$

where $E_{\text{monomer}x}$ and E_{dimer} are the total energies of the monomer x ($x = 1, 2$) and the dimer, respectively.

Using the equilibrium configurations from VASP optimization, electron density isosurfaces of the HOMO and natural population analysis of the on-site charge for all cluster monomers were calculated using PBE functional accompanied with 6-311+G(d) [57] (H to Kr) and Stuttgart/Dresden effective core potential (SDD) [58] (beyond Kr) basis sets, as implemented in the GAUSSIAN16 package [59].

Further, we considered four crystalline phases of bulk structures for 3D superatom assemblies: simple cubic (sc), body-centered cubic (bcc), face-centered cubic (fcc), and hexagonal close packed (hcp). The Brillouin zones were sampled with $4 \times 4 \times 4\boldsymbol{k}$-points grid for sc, bcc, fcc lattices, and $4 \times 4 \times 3\boldsymbol{k}$-points grid for the hcp lattice. As for 2D superatom assemblies, we considered square and hexagonal lattices and in both cases the Brillouin zone was sampled with $4 \times 4 \times 1\boldsymbol{k}$-points grid. To begin with, we carried out single-point energy calculations on the 3D and 2D superatom assemblies with a wide range of lattice parameters to obtain a reasonable range of lattice constants in the vicinity of the energy minimum. Further optimizations were performed around the equilibrium volume of each structure by fixing the cell parameters and fully relaxing the ionic positions. *Ab initio* molecular dynamics (AIMD) simulations and phonon dispersions calculations were carried out to examine the thermal and dynamic stability of 3D and 2D cluster assemblies using $2 \times 2 \times 2$ and $2 \times 2 \times 1$ supercell, respectively. The cohesive energies of 3D and 2D assemblies (E_{coh}) are calculated by

$$E_{\text{coh}} = (N \times E_{\text{cluster}} - E_{\text{assembly}})/N, \quad (2)$$

where E_{cluster} and E_{assembly} are the energies of the free Ti@Ge_{16} cluster and its assembly, respectively; N is the number of clusters in the supercell.

We have also explored metal-intercalated cluster assemblies by considering doping of X atoms from group 1 to 17 elements (H to Rn) at the edge centers, and constructed 2D compounds with stoichiometry of X_2[Ti@Ge_{16}], as well as Cs_2[Ni@Pb_{10}] and Cs_2[W@Si_{12}], which were then relaxed in terms of both cell parameters and ionic positions. As will be demonstrated later, Cs_2[Ti@Ge_{16}], Cs_2[W@Si_{12}] are found to be a Mott insulator. It is thus necessary to consider strong correlation effects due to the occurrence of very flat bands. These effects can be approximately described by adding an on-site Coulomb term for the d electrons on transition-metal atoms [60–62] into density-functional theory calculations. Here, a Hubbard-type parameter of $U_{\text{eff}} = 3$eV was selected for the d orbitals of Ti atom and $U_{\text{eff}} = 1.5$ eV for W atom, respectively. The cohesive energies of 2D metal intercalated cluster assemblies (E_{coh}') are defined as

$$E_{\text{coh}}' = (N \times E_{\text{cluster}} + 2N \times E_X - E_{\text{assembly}})/N, \quad (3)$$

where E_{cluster} and E_{assembly} are the energies of the free cluster and metal X intercalated cluster assembly, respectively; E_X is the energy of an isolated metal atom; N is the number of clusters in the supercell.

The adopted PBE-D3 scheme was supported by the benchmark calculations of fcc crystal of C_{60} fullerenes. As shown in Fig. S1 of the Supplemental Material [63],the equilibrium lattice constant (14.24 Å), cohesive energy (1.50 eV per C_{60} cage), and bulk modulus (12.33 GPa) from our calculations agree well with previous experimental and theoretical values of 14.20 Å, 1.60 eV, and 9.6 GPa, respectively [64–66].

III. RESULTS AND DISCUSSION

A. Dimers of superatoms and their assembly criteria

We considered 34 superatoms including M@Al_{12} (M = B, C, Al, Si, P), M@Si_{12} (M = Cr, W), Ru@Si_{14}, Zr@Si_{15}, M@Si_{16} (M = Sc, Ti, V, Zr, Hf), isoelectronic system with Ti@Si_{16}: alkali K-doped Sc@Si_{16} cluster and halogen F-doped V@Si_{16} or Ta@Si_{16} clusters, Th@Si_{20}, V_2@Si_{20}, M@Ge_{16} (M = Ti, Zr, Hf), M@Sn_{16} (M = Ti, Zr, Hf), M@Pb_{10} (M = Fe, Co, Ni), M@Au_{12} (M = Mo, W), Ti@Au_{14}, Ag@$Zn_{12}S_{12}$, Ag@$Zn_{16}S_{16}$, and U@B_{40}, which have been reported in the previous studies [9,21–45]. For each cluster, we constructed a dimer from two monomers. As an exception, Sc@Si_{16} and V@Si_{16} were selected to form a dimer, considering their total number of valence

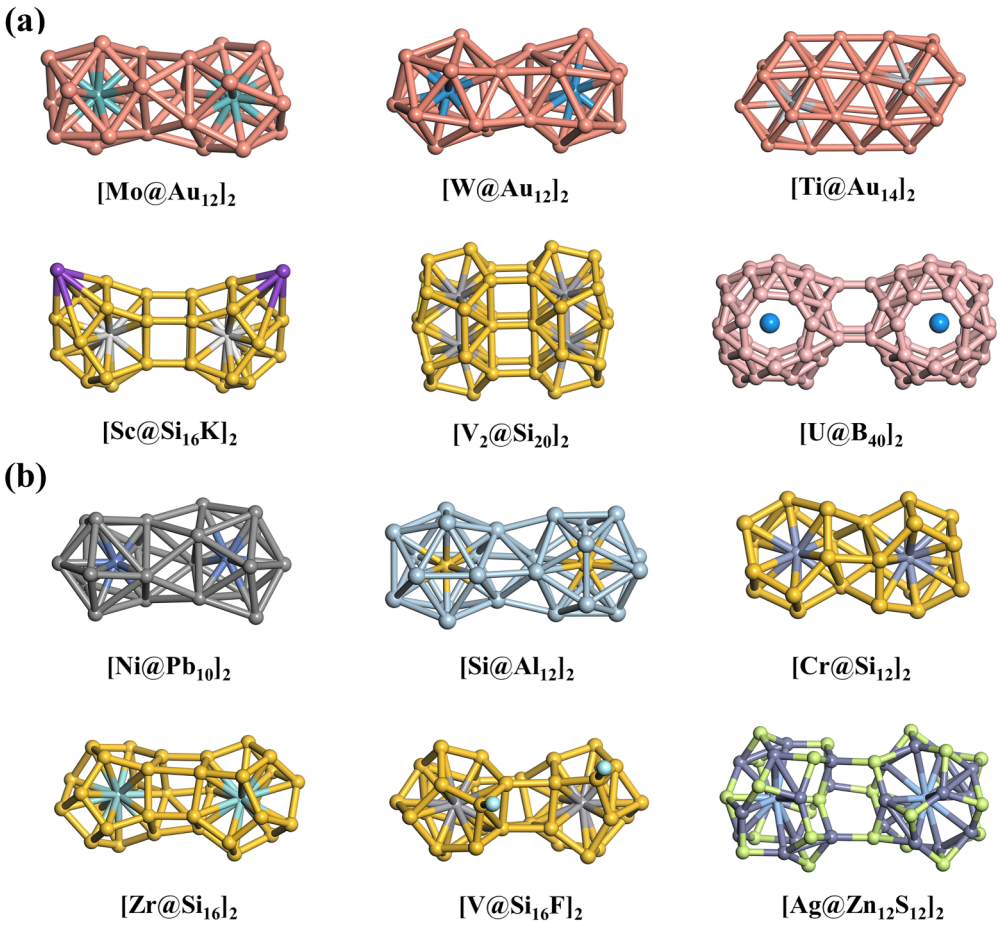

FIG. 1. Lowest-energy structures of selected superatom cluster dimers with dimerization energies (a) larger than 3.0 eV and (b) between 1.0 and 3.0 eV. The corresponding geometric and electronic properties are given by Table I.

electrons just satisfies a closed electronic shell. The structures and dimeric interaction of the constructed 33 superatom dimers are presented in Fig. 1, Table I, Table S1, and Fig. S2. According to the dimerization energy, superatom dimers can be divided into three types: (i) those with strong interaction ($E_E > 3.0$eV), (ii) with intermediate interaction ($0.4\text{eV} \leqslant E_d \leqslant 3.0\text{eV}$), and (iii) with vdW-type interaction ($E_d < 0.4$eV). As one can see in Fig. 1(a), many endohedrally doped clusters with cagelike geometry and closed electronic shell, such as $Mo@Au_{12}$, $W@Au_{12}$, $Ti@Au_{14}$, $Sc@Si_{16}K$, $V_2@Si_{20}$, $U@B_{40}$, interact rather strongly ($E_d > 3$eV) with each other by forming intercluster covalent bonds. In comparison, cluster dimers composed of $Ni@Pb_{10}$, $Si@Al_{12}$, $Cr@Si_{12}$, $Ru@Si_{14}$, $Zr@Si_{16}$, $V@Si_{16}F$, or $Ag@Zn_{12}S_{12}$ interact relatively weakly such that the cluster monomers almost keep their geometries but form some covalent bonds between each other, as displayed in Fig. 1(b). Consequently, the structural identity and unique electronic properties of individual cluster cannot be fully retained in these two categories of cluster dimers (and consequently also in other forms of assemblies), consistent with previous theoretical studies [46,48,50,67–69]. For a dimer formed by two magnetic clusters, either ferromagnetic (e.g. $[Fe@Pb_{10}]_2$) or antiferromagnetic coupling (e.g., $[Cr@Si_{12}]_2$ and $[U@B_{40}]_2$) is found. As shown in Fig. 2(a), Table I, and Table S1, only dimerization energies of $[Ti@Si_{16}]_2$, $[M@Ge_{16}]_2$ (M = Ti, Zr, Hf) and $[M@Sn_{16}]_2$ (M = Ti, Zr, Hf) are weak enough ($E_d = 0.26$–0.49 eV) to be considered as the vdW type, in agreement with the previous finding by Kumar and Kawazoe [29,30]. The large intercluster distances of over 3.4 Å further manifest that there is no covalent bonding between the two clusters. Moreover, the sizable HOMO-LUMO gap of individual $Ti@Si_{16}$, $M@Ge_{16}$ (M = Ti, Zr, Hf), and $M@Sn_{16}$ (M = Ti, Zr, Hf) cluster is only moderately reduced by about 0.35−0.53 eV when they form a dimer (see Table I and Table S1). Therefore, $Ti@Si_{16}$, $M@Ge_{16}$ (M = Ti, Zr, Hf), and $M@Sn_{16}$ (M = Ti, Zr, Hf) clusters with the FK polyhedron cage structures are candidate 0D Lego blocks for assembling nanostructures of different dimensionalities.

To confirm the above results, we further calculated the kinetic barriers for two cluster monomers to approach each other to make up a covalently bonded dimer. $W@Au_{12}$ and $U@B_{40}$, $Ni@Pb_{10}$, $Si@Al_{12}$, and $Zr@Si_{16}$, as well as $Ti@Ge_{16}$ were selected as representatives that have strong, intermediate, and vdW-type interactions in their dimer forms, respectively. The energy profile as a function of intercluster distance is given by Fig. S3. For $W@Au_{12}$, $U@B_{40}$, $Ni@Pb_{10}$, and $Si@Al_{12}$, as the two monomers are brought to each other, they agglomerate into dimeric species by forming covalent bonds between clusters without any barrier. Dimerization of $Zr@Si_{16}$ involves a small energy barrier of 0.10 eV. Surprisingly, two $Ti@Ge_{16}$ monomers, which are initially placed at a distance of only

TABLE I. Geometric and electronic properties of selected superatom clusters, including symmetry (Sym.), average bond length of surface atoms (R), HOMO-LUMO gap ($E_{\mathrm{H-L}}$), average on-site charge of surface atoms (Q), average coordination number (CN) of surface atoms, and average coordination number (CN′) of pure cluster of the same size without endohedral doping (their ground-state structures are taken from the references cited below). Shortest distance (D), dimerization energy (E_{d}), HOMO-LUMO gap ($E_{\mathrm{H-L}}$), and magnetic state are listed for the cluster dimers. The notations of "FM" and "AFM" stand for ferromagnetic and antiferromagnetic coupling between two clusters in a dimer, respectively.

	Monomer						Dimer			
System	Sym.	R (Å)	$E_{H-\mathrm{L}}$(eV)	Q ($\|e\|$)	CN	CN′	D (Å)	E_{d} (eV)	$E_{H-\mathrm{L}}$(eV)	Mag.
$Ni@Pb_{10}$	D_{4d}	3.29	0.85	0.23	5.8	4.9[a]	3.19	1.22	0.73	
$Si@Al_{12}$	I_h	2.77	2.01	0.14	6	6[b]	2.71	2.12	0.62	
$Cr@Si_{12}$	D_{6h}	2.35	0.87	0.28	4	4.3[c]	2.28	1.97	0.65	AFM
$Mo@Au_{12}$	O_h	2.58	0.25	0.38	5	5[d]	2.73	4.62	0.49	
$W@Au_{12}$	I_h	2.88	1.79	0.40	6	5[d]	2.73	4.47	0.52	
$Ti@Au_{14}$	D_{4d}	2.82	1.38	0.39	5.3	5.5[e]	2.72	4.67	0.38	FM
$Ti@Si_{16}$	T_d	2.37	2.36	0.28	6.3	4.2[c]	3.45	0.26	1.90	
$Zr@Si_{16}$	D_{4d}	2.33	1.57	0.25	4	4.2[c]	2.41	2.14	0.49	
$Ti@Ge_{16}$	T_d	2.75	1.76	0.26	6.3	5[f]	3.80	0.31	1.41	
$Ti@Sn_{16}$	T_d	3.10	1.27	0.26	6.3	5.7[g]	3.77	0.49	0.83	
$Sc@Si_{16}K$	C_s	2.33	1.11	0.13 (0.93)[h]	4.1	4.4[c]	2.35	3.61	0.33	
$V@Si_{16}F$	C_s	2.33	1.49	0.19 (−0.61)[i]	3.8	4.4[c]	2.44	1.89	0.65	
$V_2@Si_{20}$	C_{2h}	2.39	0.91	0.33	4.7	4.4[j]	2.34	4.66	0.77	
$Ag@Zn_{12}S_{12}$	T_d	2.85 (2.30)[k]	0.31	0.86 (−0.83)[l]	4		2.35	1.97	2.00	
$U@B_{40}$	D_{2d}	1.69	0.72	0.07	4.6	4.6[m]	1.73	5.09	0.48	AFM

[a]Reference [93].
[b]Reference [94].
[c]Reference [95].
[d]Reference [96].
[e]Reference [97].
[f]Reference [98].
[g]Reference [99].
[h]Natural population analysis charge of K atom.
[i]Natural population analysis charge of F atom.
[j]Reference [100].
[k]Average bond length between Zn and S atoms.
[l]Average natural population analysis charge of S atoms.
[m]Reference [101].

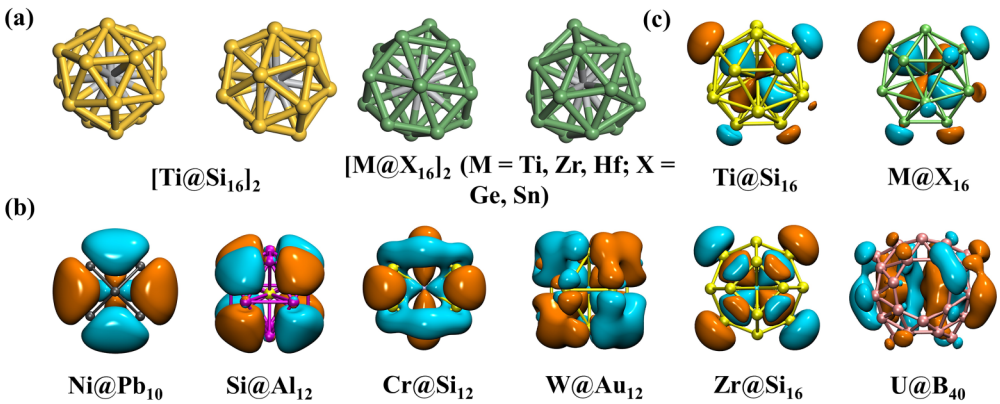

FIG. 2. (a) Lowest-energy structures of $[Ti@Si_{16}]_2$, $[M@Ge_{16}]_2$, and $[M@Sn_{16}]_2$ (M = Ti, Zr, Hr) dimers with vdW interaction. (b), (c) Electron density isosurfaces of the HOMOs of various superatom clusters, with isosurface value of 0.01 a.u. for $Ni@Pb_{10}$, 0.02 a.u. for $Si@Al_{12}$, $Zr@Si_{16}$, and $U@B_{40}$, 0.015 a.u. for $Cr@Si_{12}$ and $W@Au_{12}$, and 0.034 a.u. for $Ti@Si_{16}$, $M@Ge_{16}$ and $M@Sn_{16}$ clusters. The orange and cyan colors stand for positive and negative wave function, respectively.

2.3 Å, would repulse from each other upon structure optimization and relax to a vdW interaction distance of 3.8 Å, with energy lowered by over 6 eV.

To gain further insights into the nature of cluster-cluster interaction, we thoroughly analyzed the geometric and electronic properties of all the considered cluster monomers given in Table I and Table S1. The criteria for clusters to serve as building blocks have been derived. First, the cluster should have both closed electronic shell and closed atomic shell. To satisfy this criterion, endohedral cages with precisely controlled number of valence electrons are usually preferred [9]. Second, the surface atoms of the cluster should have (nearly) the same charge state. As a counterexample, $Ag@Zn_{12}S_{12}$ carries charges of $0.86|e|$ on each Zn atom and $-0.83|e|$ on S atom, which lead to strong Coulomb attraction between the positively charged Zn atoms and negatively charged S atoms between the two clusters in the $[Ag@Zn_{12}S_{12}]$ dimer. As a consequence, there is a substantial dimerization energy of 1.97 eV (see Table I). Third, the electron cloud of the HOMO should be trapped within the cage and distributed around the endohedral atom as much as possible. As the highest occupied frontier orbital of a cluster, there is considerable overlap of the HOMOs of the two clusters. This usually leads to rather strong intercluster interaction. To directly visualize this effect, we drew the electron density isosurfaces for the HOMO of the considered clusters in Figs. 2(b) and 2(c) and Fig. S4. When two cage clusters form a dimer, then clusters with delocalized HOMO on the cage surface are easier to aggregate as in the case of $M@Pb_{10}$ (M = Fe, Co, Ni), $M@Al_{12}$ (M = C, Si), $M@Si_{12}$ (M = Cr, W), and $M@Au_{12}$ (M = Mo, W). On the contrary, clusters having HOMO mainly distributed inside the cage, e.g., $Ti@Si_{16}$, $M@Ge_{16}$ (M = Ti, Zr, Hf), and $M@Sn_{16}$ (M = Ti, Zr, Hf) interact weakly with each other and can retain their identity. Finally, the average coordination number of the surface atoms of endohedrally doped cluster should be larger than that of the undoped cluster of the same size in its ground state. This increased coordination as well as a strong hybridization between the orbitals of the endohedral atom and the HOMO of the outer cage will weaken the reactivity of the cluster, such that the formation of covalent bonds between two endohedrally doped clusters may be unfavorable. A comparison of average coordination numbers between doped and undoped clusters is given by Table I, Table S1, and Fig. S5, showing that $M@Pb_{10}$ (M = Fe, Co, Ni), $M@Au_{12}$ (M = Mo, W), $Ti@Si_{16}$, $M@Ge_{16}$ (M = Ti, Zr, Hf), and $M@Sn_{16}$ (M = Ti, Zr, Hf) fulfill this requirement. Considering the above four criteria together, $Ti@Si_{16}$, $M@Ge_{16}$ (M = Ti, Zr, Hf), and $M@Sn_{16}$ (M = Ti, Zr, Hf) clusters meet all of them, in good coincidence with the results from our computational screening of the 33 cluster dimers.

B. 3D and 2D assemblies of $Ti@Ge_{16}$ clusters

We used $Ti@Si_{16}$, $M@Ge_{16}$ (M = Ti, Zr, Hf), and $M@Sn_{16}$ (M = Ti, Zr, Hf) superatoms as potential building blocks for assembling 3D materials. As shown in Fig. S6, the $Ti@Si_{16}$, $M@Ge_{16}$ (M = Zr, Hf), and $M@Sn_{16}$ (M = Ti, Zr, Hf) clusters show covalent bonds between cages in sc lattices, which disagree with the vdW type of bonding between clusters in $Ti@Si_{16}$ solid in previous studies [70–72]. Only $Ti@Ge_{16}$ has outstanding stability and is qualified as the 0D Lego block for constructing vdW solids. Compared with cluster dimers, the requirement of the cluster's stability is more stringent in cluster-assembled solids due to the increase of neighboring cages. Intuitively, we speculate that the clusters having no low-energy isomers (details in Fig. S6) and meanwhile having uniform charge distribution are more favorable for assembling vdW solids (see localized orbital locator [73] patterns in Fig. S7).

We considered sc, bcc, hcp, and fcc phases of $Ti@Ge_{16}$ assembled 3D solids and computed the cohesive energy as a function of cell volume as plotted in Fig. 3(a) and Fig. S8. For each data point, the ionic positions of the clusters at a fixed cell parameter were fully relaxed. These results show that fcc is the most stable phase for the assembled 3D solids of $Ti@Ge_{16}$ with the largest cohesive energy of 1.76 eV per cage (compared to 1.50 eV per cage for C_{60} solid) and equilibrium lattice parameter of 12.10 Å. The energy-volume (E-V) curve fitted from the Birch-Murnaghan equation of state yields a rather low bulk modulus of 4.96 GPa, which is less than half the value for C_{60} solid. The equilibrium structure of fcc $Ti@Ge_{16}$ superatom crystal is shown in Fig. 3(b). The separation between the superatoms is 3.04 Å, suggesting that there is no covalent bonding between the neighboring superatoms in the crystal. Moreover, upon assembling, the atom rearrangements within each cluster are negligible compared to the isolated cluster geometry: the average Ti−Ge (Ge−Ge) bond lengths remain almost intact with the value of 2.98 Å (2.77 Å) compared with the value of 2.99 Å (2.75 Å) in free $Ti@Ge_{16}$ cluster.

For the 2D assemblies of $Ti@Ge_{16}$ superatoms, we considered two possible phases with hexagonal and square lattices. As shown in Fig. 3(c) and Fig. 3(d), the cohesive energy in the 2D hexagonal lattice is higher with the value of 0.85 eV per cage and an equilibrium lattice parameter of 8.60 Å. The separation between clusters is 3.22 Å, slightly larger than the 3D case. The average Ti−Ge (Ge−Ge) bond length is 2.98 Å (2.74 Å) in this 2D assembly, very close to that of the free $Ti@Ge_{16}$ cluster. For the 2D square lattice, the cohesive energy is 0.65 eV per cage, the equilibrium lattice parameter is 8.50 Å, and intercluster separation is 3.35 Å. Despite its metastable nature, the assembly with a square lattice offers a playground for intercalating metal atoms between the clusters, as we shall discuss in the following subsection.

For both 3D and 2D assemblies, we further fully optimized their crystal structures for both ionic and cell degrees of freedom, by starting from the equilibrium 3D fcc and 2D hexagonal lattices in Figs. 3(b) and 3(d), respectively. These two superatom crystals almost keep their fcc or hexagonal geometries, with the lattice constant changed by only 3 and 1%, respectively. The variations in bond lengths, cohesive energies, and band gap upon relaxation of cell parameters are listed in Table II, all of which are minor changes (less than 0.02 Å, 0.1 eV, and 0.11 eV, respectively). The geometries and electronic band structures are displayed in Fig. S9 for reference. The elastic constants were computed for these fully optimized 3D and 2D crystals of $Ti@Ge_{16}$ (Table S2). The nonzero elastic constants satisfy the Born stability criteria [74],manifesting the mechanical stability of these cluster assemblies.

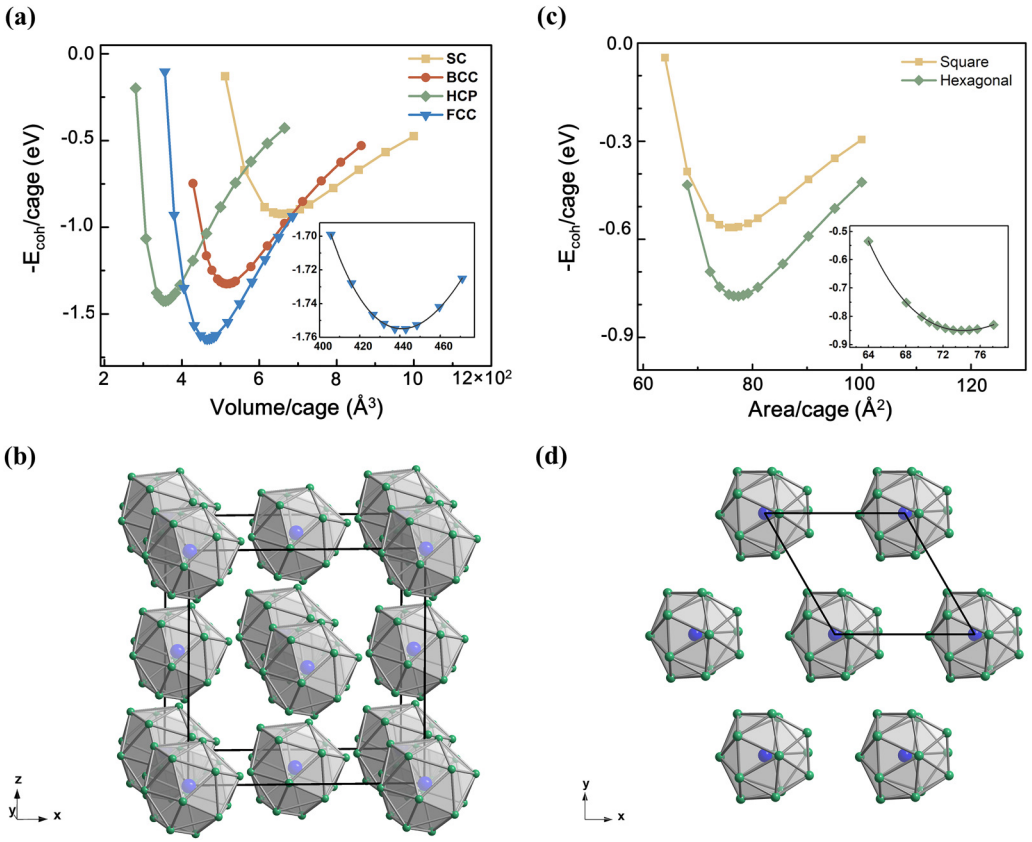

FIG. 3. (a) Cohesive energy vs volume (E-V) curve for 3D Ti@Ge_{16} superatom crystal from single-point energy calculations. (b) Equilibrium structure of fcc crystal of Ti@Ge_{16} with lattice constant of 12.10 Å. (c) Cohesive energy vs area (E-A) curve for 2D Ti@Ge_{16} superatom assembly from single-point energy calculations. (d) Equilibrium structure of 2D hexagonal lattice of Ti@Ge_{16} with lattice constant of 8.60 Å. The insets in (a) and (c) show the E-V (E-A) curves from cluster assemblies by full ions optimization. The data points are fitted to Birch-Murnaghan equation of state (dark gray lines). The black boxes in (b) and (d) indicate the unit cell of cluster assemblies.

The thermal stabilities of the cluster assemblies were evaluated by AIMD simulations. For the 3D fcc crystal of Ti@Ge_{16}, the assembled structure is well maintained at 77 K for simulation time up to 5 ps (see Fig. S10). The clusters keep their identities with the intercluster distance above 2.95 Å. From 8 to 20 ps, some Ge atoms dissolve from the clusters; nevertheless, most clusters preserve their cage structures without agglomeration. The 2D hexagonal lattice of Ti@Ge_{16} exhibits outstanding stability even at 300 K, without noticeable deformation during a simulation time of 20 ps (see Fig. S11). The clusters in the 2D assembly are well separated by 3.12 Å.

The phonon dispersions of the superatom lattices were also calculated to examine their dynamic stability. As shown in Fig. S12, an imaginary band occurs at small frequency of about $-8\,\mathrm{cm}^{-1}$ for both 2D and 3D cluster assemblies. Such small negative phonon frequency may be ascribed to the insufficient optimization of relative orientations of cage clusters in their assembled solids, as we considered only the unit cell for constructing the 3D fcc and 2D hexagonal lattices of Ti@Ge_{16}. Deposition on proper substrates may help stabilize the cluster-assembled nanostructures and remove the imaginary phonon bands.

TABLE II. Geometric, energetic, and electronic properties of 3D fcc and 2D hexagonal lattices of Ti@Ge_{16}, including lattice constants (a, b, c), lattice angles (θ_α, θ_β, θ_γ), average Ti−Ge bond length ($R_{\mathrm{Ti-Ge}}$) and Ge−Ge bond length ($R_{\mathrm{Ge-Ge}}$), cohesive energy (E_{coh}), and band gap (E_{g}). These crystal structures are optimized by either fixing (3D-fcc, 2D-hexa.) or relaxing the cell parameters (3D, 2D). The notation of "i" and "d" for E_{g} represent indirect and direct band gap, respectively.

System	a	b	c	θ_α	θ_β	θ_γ	$R_{\mathrm{Ti-Ge}}$	$R_{\mathrm{Ge-Ge}}$	E_{coh}	E_{g}
	(Å)			(°)			(Å)		(eV)	
3D-fcc	12.10	12.10	12.10	90	90	90	2.99	2.75	1.76	0.29 (d)
3D	11.63	11.64	12.43	89.9	89.9	90.6	2.98	2.77	1.86	0.18 (d)
2D-hexa.	8.60	8.60				120	2.98	2.75	0.85	1.00 (i)
2D	8.50	8.74				120	2.98	2.74	0.85	0.90 (i)

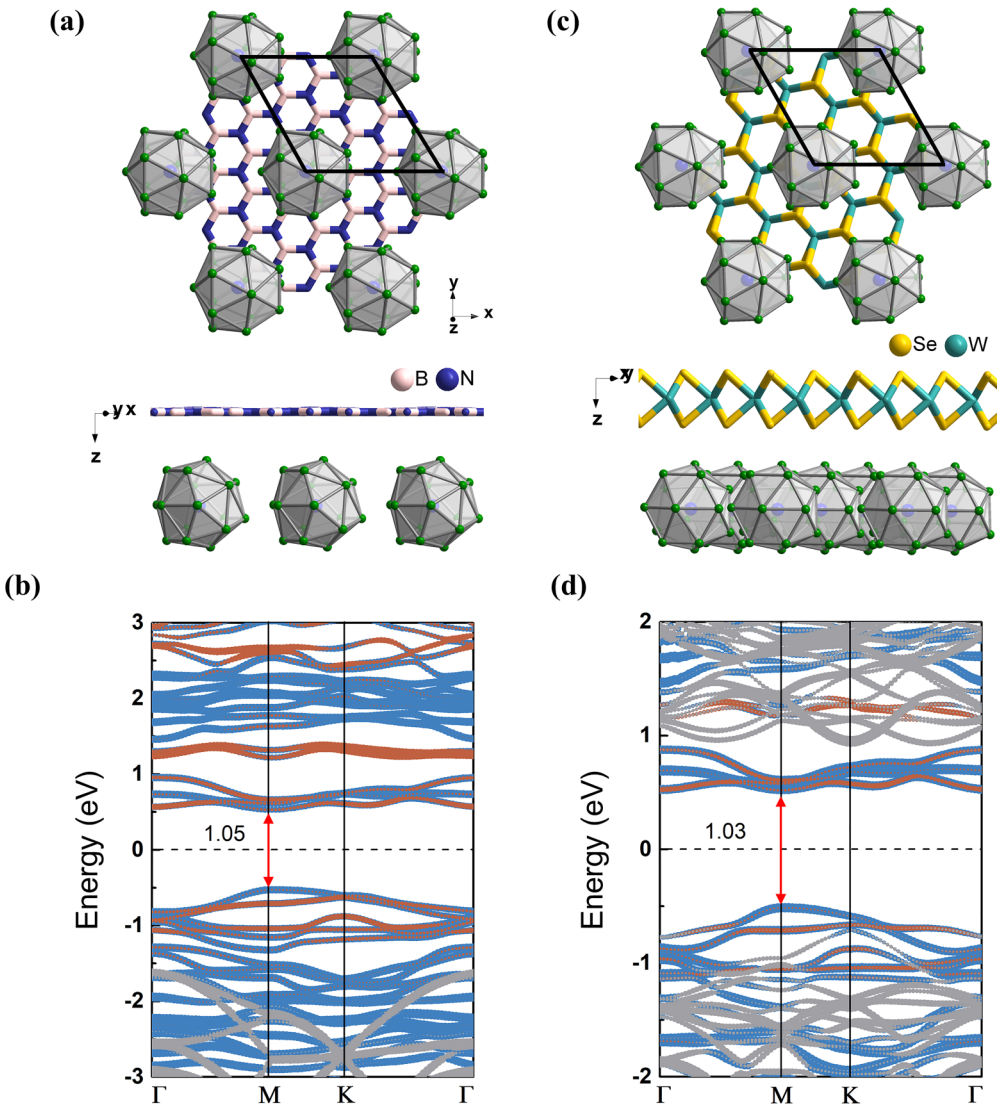

FIG. 4. (a) Geometric structure and (b) electronic band structure of 2D Ti@Ge_{16} lattice on *h*-BN monolayer. (c) Geometric structure and (d) electronic band structure of 2D Ti@Ge_{16} lattice on WSe_2 monolayer. The electronic bands from Ti and Ge atoms, and substrate are shown in red, blue, and gray colors, respectively. The black number and red arrow indicate band gap. The Fermi level (dashed line) is set to zero.

Stimulated by the experimental progress in fabrication of 2D arrays of precisely selected clusters on appropriate substrates [12,13,75–80], we placed the 2D hexagonal Ti@Ge_{16} assembly on selected 2D vdW materials, including *h*-BN [81,82], and Mo as well as W dichalcogenides monolayer [83,84]. These substrates have excellent stability, large band gap, and small lattice mismatch with the 2D hexagonal Ti@Ge_{16} lattice (about 1%). As presented in Fig. 4 and Table S3, the 2D superatom lattice does not change by the substrate interaction, and its band gap remains intact.

The evolution behavior of the electronic structure from cluster monomer to 2D hexagonal and 3D fcc assemblies is revealed in Fig. 5. For an empty Ge_{16} cage with T_d symmetry, the irreducible representation of its HOMO is t_2, meaning that this energy level is triply degenerate [see Fig. 5(a)] and is able to host up to six electrons. However, Ge_{16} can afford only two electrons to occupy the HOMO. After endohedral doping, the central Ti atom provides the remaining four valence electrons to fully fill the triply degenerate t_2 orbitals of Ge_{16} cage, rendering the doped cluster to satisfy a 68-electron closed shell within the picture of the spherical jellium model [85]. Further analyses reveal that the 3*d* orbitals of Ti atom hybridize mainly with the 4*p* orbitals of Ge atoms to form the HOMO and LUMO levels of Ti@Ge_{16} cluster or the conduction-band minimum and valence-band maximum of the 3D and 2D assemblies (see Fig. S13 for details). With increasing number of neighboring clusters, the HOMO-LUMO gap of Ti@Ge_{16} gradually reduces from 1.76 eV for a monomer to 1.41 eV for a dimer, then to an indirect band gap of 1.00 eV (0.97 eV) for the 2D hexagonal (square) lattice, and finally to a direct band gap of 0.29 eV for 3D fcc solid, signifying the increasing impact of cluster-cluster interaction on the electronic structure of the assembled solids.

C. Intercalation of 2D superatom assemblies

Intercalation in 2D assemblies of superatoms provides another opportunity to design nanostructures with peculiar

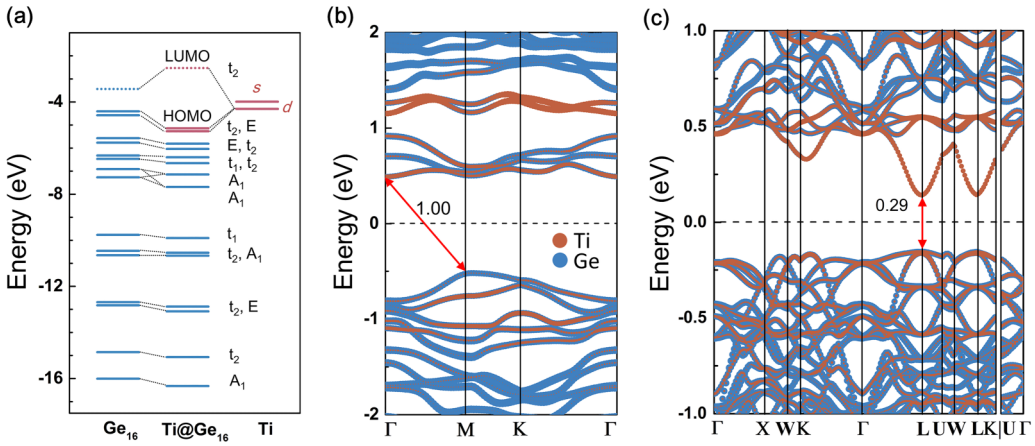

FIG. 5. (a) Correlation between the orbital levels of Ti and Ge_{16} fragments in $Ti@Ge_{16}$. The irreducible representation for orbitals is given next to their energy levels. The vacuum level is set to zero. (b) Electronic band structures of 2D hexagonal and (c) 3D fcc lattices of $Ti@Ge_{16}$. The contributions from Ti and Ge are shown in red and blue colors, respectively. The black number and red arrow indicate band gap. The Fermi level (dashed line) is set to zero.

electronic properties in a way similar to the fullerides. For 2D materials, there have been some efforts to dope transition-metal atoms in graphene [86], *h*-BN [87], phosphorene [88], and borophene [89] monolayers, leading to the possibility to induce local spin moments, enhance superconductivity, and trigger novel electronic phases such as magnetic semiconductors and half metals [90]. Inspired by such 2D materials, one can utilize 2D crystal of $Ti@Ge_{16}$ clusters with a square

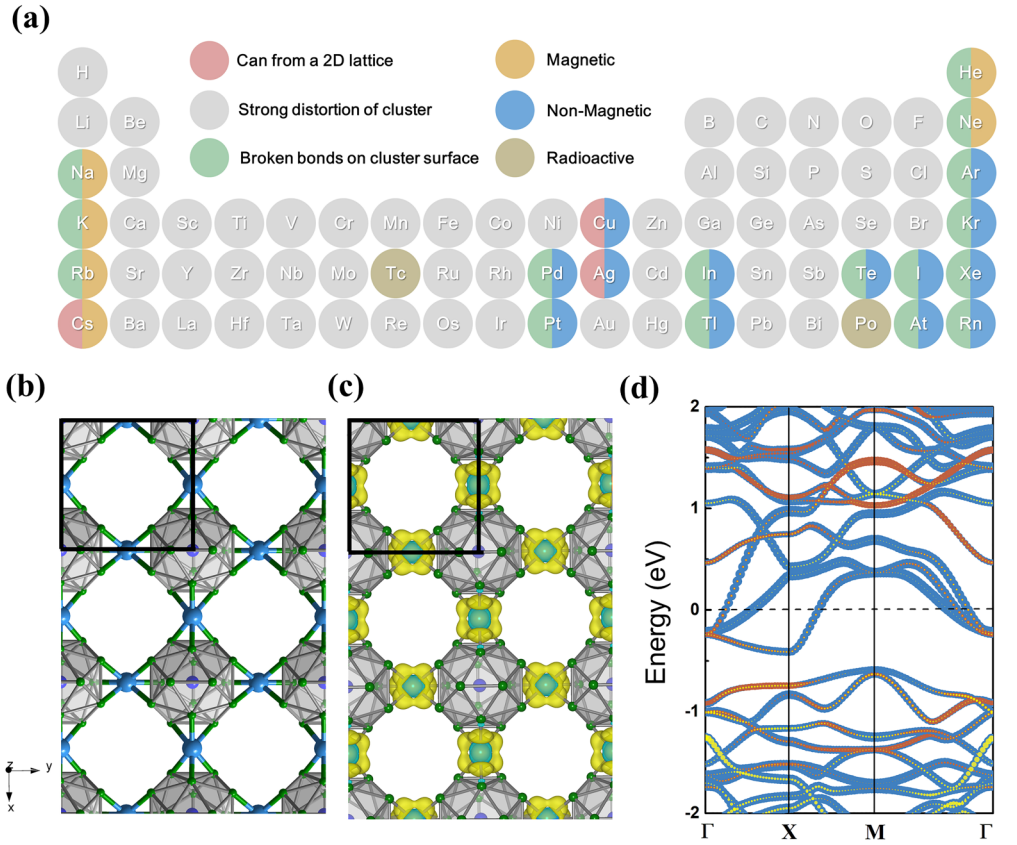

FIG. 6. (a) Structural and electronic information of edge-intercalated 2D assembly of $Ti@Ge_{16}$ using different elements from the periodic table. Radioactive elements Tc and Po are not considered in this work. (b) Geometric structure, (c) differential charge density, and (d) electronic band structure of 2D lattice of $Cu_2[Ti@Ge_{16}]$. Cu atoms are shown in blue. The differential charge density is relative to the 2D $Ti@Ge_{16}$ lattice and intercalated Cu atoms. The yellow and cyan colors represent electron accumulation and depletion regions with isosurface value of 0.001 a.u., respectively. The electronic bands from Ti, Ge, and Cu atoms are shown in red, blue, and yellow colors, respectively. The Fermi level (dashed line) is set to zero.

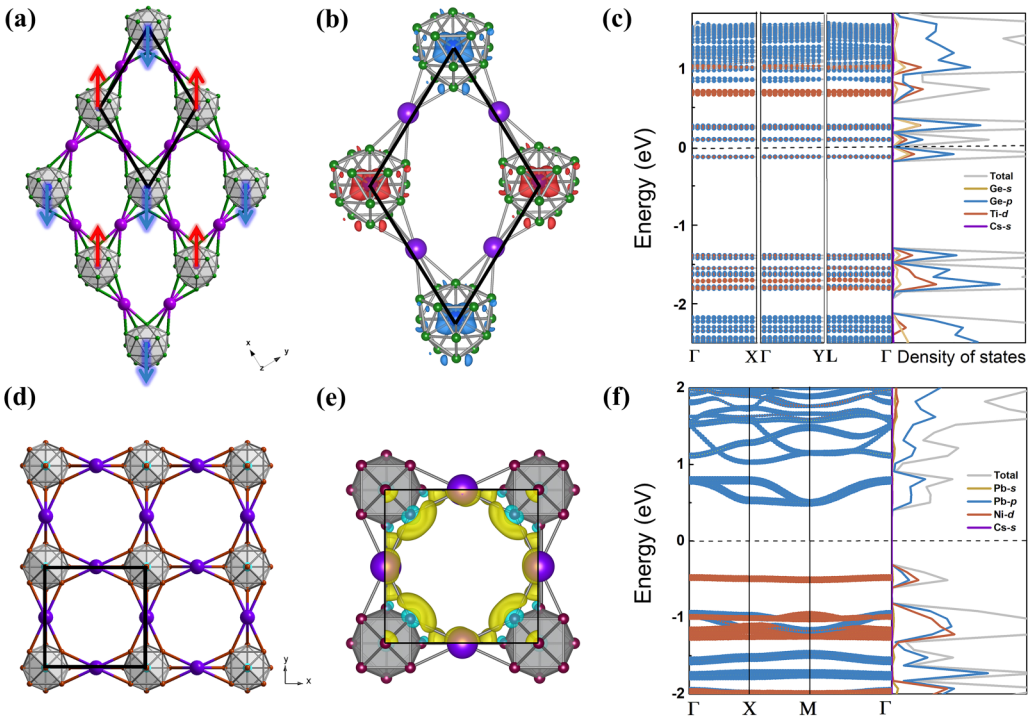

FIG. 7. (a) Geometric structure, (b) spin density, and (c) electronic band structure (left panel) and density of states (right panel) of 2D lattice of $Cs_2[Ti@Ge_{16}]$. Spin density in red stands for spin up and blue is for spin down. (d) Geometric structure, (e) differential charge density (isosurface value of 0.001 a.u.), and (f) electronic band structure (left panel) and density of states (right panel) of 2D lattice of $Cs_2[Ni@Pb_{10}]$. The Fermi level (dashed line) is set to zero.

lattice as a template to further construct intercalated compounds with an X atom at each edge center of the superatomic lattice. In this work, we have explored all possible dopant elements (X ranging from H to Rn) and fully optimized the resulting $X_2[Ti@Ge_{16}]$ 2D structures. Upon relaxation, it is found that three intercalated systems remain stable, including 2D compounds of $Cu_2[Ti@Ge_{16}]$, $Ag_2[Ti@Ge_{16}]$, and $Cs_2[Ti@Ge_{16}]$.

As shown in Figs. 6(b) and 6(c), $Cu_2[Ti@Ge_{16}]$ and $Ag_2[Ti@Ge_{16}]$ lattices have square shape with doped Cu/Ag atoms located at the edge centers. The cohesive energies are 8.08 and 5.32 eV for $Cu_2[Ti@Ge_{16}]$ and $Ag_2[Ti@Ge_{16}]$ lattices, respectively, significantly higher than that of 2D squared lattice of $Ti@Ge_{16}$ (0.65 eV). The remarkably enhanced stability is attributed to the six Cu–Ge or Ag–Ge bonds formed between metal dopant and two neighboring clusters. As $Ti@Ge_{16}$ has a 68-electron closed electronic shell, the intercalated Cu and Ag atoms serve as donor impurities in its 2D assembly. The electronic band structures in Fig. 6(d) and Figs. S14 and S15 show that the donated electrons from intercalated metal atoms fill some conduction bands of the original 2D $Ti@Ge_{16}$ crystal, converting it to n-type semiconductor with gap of 0.17 and 0.72 eV below the Fermi level for the Cu and Ag intercalated systems, respectively.

The 2D lattice of $Cs_2[Ti@Ge_{16}]$ becomes a hexagonal shape upon structure optimization, as depicted in Fig. 7. The cohesive energy is 3.96 eV. Compared with Cu and Ag atoms, Cs atom has the lowest electronegativity such that each $Ti@Ge_{16}$ cluster gains 1.6 electrons from two Cs atoms according to Bader charge analysis (0.7 and 0.9 electrons on the Ge_{16} cage and endohedral Ti atom, respectively). The charge transfer from the intercalated Cs atoms induces a magnetic moment of 1.6 μ_B on $Ti@Ge_{16}$ cluster (0.7 μ_B carried by the cage and 0.9 μ_B by Ti atom). Intriguingly, the magnetic moments on neighboring $Ti@Ge_{16}$ clusters are coupled antiferromagnetically. Moreover, the large radius of Cs atoms leads to weak cage-cage interaction, as indicated by the intercage distance over 7 Å (see Table III), which prevents the overlap of wave functions between clusters. As a result, the 2D $Cs_2[Ti@Ge_{16}]$ assembly exhibits strong localization behavior with nearly flat bands and has a reduced band gap of 0.22 eV due to the filling of LUMO of $Ti@Ge_{16}$ by the transferred electrons from Cs atoms (Fig. 7). Therefore, the 2D superatom lattice of $Cs_2[Ti@Ge_{16}]$ can be regarded as a typical antiferromagnetic Mott insulator [91].

Based on these exciting results, we also explored the possibilities of metal-intercalated 2D assemblies using the clusters with strong dimeric interaction. Specifically, we considered two superatoms $Ni@Pb_{10}$ $Ni@Pb_{10}$ and $W@Si_{12}$ with dimerization energies of 1.22 and 1.66 eV, respectively. They form covalent bonds in the dimers and their cage structures encounter severe distortion when assembled into 2D lattices. Encouragingly, the 2D assemblies of these two clusters can be stabilized by intercalating proper metal atoms at the edge center. Considering Cs intercalation as a representative, we calculated the geometries and electronic band structures of 2D $Cs_2[W@Si_{12}]$ and $Cs_2[Nb@Pb_{10}]$ assemblies. Similar to $Cs_2[Ti@Ge_{16}]$, the $W@Si_{12}$ cluster with 18-electron closed shell gains 1.6 electrons from the intercalated Cs atoms and forms a hexagonal 2D lattice. These transferred electrons are localized on clusters and induce magnetic moments of 1.2 μ_B

TABLE III. Geometric and electronic properties of metal-intercalated 2D lattices of superatom clusters, including lattice constants (a, b), lattice angle (θ_γ), average bond length between endohedral metal M and surface atoms of cluster S (R_{M-S}), average bond length between surface atoms (R_{S-S}) shortest distance between intercalated atom X and cluster (D_{X-S}), Bader charge on doped metal atom (Q), cohesive energy per cage (E_{coh}), band gap (E_g), and magnetic state (Mag.). Negative charge means electron transfer from cluster to the endohedral metal atom. The notation of "*i*," "*d*," "*n*," for E_g represent indirect, direct, and *n*-type semiconductor, respectively.

System	a (Å)	b	θ_γ (°)	R_{M-S}	R_{S-S} (Å)	D_{X-S}	Q (|e|)	E_{coh}	E_g (eV)	Mag.
$Cu_2[Ti@Ge_{16}]$	8.66	8.66	90	2.87	2.77	2.45	−0.05	8.08	0.00 (*n*)	
$Ag_2[Ti@Ge_{16}]$	9.11	9.11	90	2.88	2.77	2.63	−0.08	5.32	0.00 (*n*)	
$Cs_2[Ti@Ge_{16}]$	11.81	11.76	116	2.97	2.76	3.73	0.80	3.96	0.22 (*d*)	AFM
$Cs_2[W@Si_{12}]$	11.21	11.18	109	2.66	2.40	3.80	0.85	5.05	0.29 (*d*)	AFM
$Cs_2[Ni@Pb_{10}]$	10.68	10.68	90	2.88	3.27	4.02	0.75	4.69	0.98 (*i*)	

that are antiferromagnetically aligned between the neighboring clusters. As a result, 2D $Cs_2[W@Si_{12}]$ assembly is also an antiferromagnetic Mott insulator with a band gap of 0.29 eV (Figs. S16 and S17).

On the other hand, the $Ni@Pb_{10}$ cluster is a 10-vertex closed deltahedron with 20 valence electrons according to the Wade-Mingos rules. It needs two more electrons for skeletal bonding of molecular orbitals to satisfy the $2n + 2$ ($n = 10$) frameworks with closed geometric shell, just as the synthetic $[Ni@Pb_{10}]^{2-}$ in Zintl compounds with remarkable stability [92]. Each intercalated Cs atom donates about one electron to the $Ni@Pb_{10}$ cluster, which helps close its electronic shell. Consequently, the $Cs_2[Nb@Pb_{10}]$ assembly forms a stable 2D square lattice, opening up an indirect band gap of 0.98 eV that is even larger than the HOMO-LUMO gap of 0.85 eV for the $Ni@Pb_{10}$ monomer [Fig. 7(f), Table I].

To sum up, intercalation of metal atoms offer a flexible strategy to achieve stable 2D superatom lattices with designable physical properties. Not only the cage clusters having weak vdW interaction, but also those forming strong covalent bonds in the dimers can be stabilized in 2D lattices by intercalating proper metal atoms at the edge center. In addition, the charge transfer from intercalated metal atoms allows adjusting the electronic configuration of clusters, thus opening more opportunities to develop cluster assemblies nanostructures with diverse electronic band structures and exotic quantum states.

IV. CONCLUSION

In summary, we have proposed the criteria for designing weakly interacting clusters as Lego blocks for assembling materials by examining the properties and dimeric interaction of 34 superatom cage clusters. Remarkably, the desired superatoms to be used as building blocks of materials should satisfy not only the requirement of doubly closed shell of atomic and electronic structures, but also have a nearly uniform charge distribution and high coordination number of the surface atoms, as well as the HOMO orbital and electron distribution of the whole cluster should mainly be localized within the cage. The $Ti@Ge_{16}$ cluster is screened as a candidate building block, and its 3D and 2D assemblies favor the fcc crystal and hexagonal packing, respectively. All the superatom-assembled crystals are semiconductors with the band gap decreasing as the material dimensionality increases. Remarkably, intercalation of metal atoms (e.g. Cu, Ag, Cs) provides a flexible scheme to obtain stable 2D superatom lattices for not only the clusters with weak vdW interaction but also those forming strong covalent bonds in the dimers. Selecting proper metal elements allows precise modulation of the electronic configuration of the cluster, endowing 2D cluster assemblies with rich physical properties from intrinsic or doped semiconductor to antiferromagnetic Mott insulator. These theoretical results provides vital guidance for selecting suitable 0D building blocks towards experimental synthesis of self-assembled crystals of superatoms, shining light on designing 2D and 3D arrays of superatoms with exotic quantum states.

ACKNOWLEDGMENTS

This work was supported by the National Natural Science Foundation of China (Grants No. 11974068 and No. 91961204), the Fundamental Research Funds for the Central Universities of China (Grants No. DUT20LAB110 and No. DUT20LAB203). The authors acknowledge the computer resources provided by the Shanghai Supercomputer Center and the Supercomputing Center of Dalian University of Technology.

[1] A. K. Geim and I. V. Grigorieva, Nature (London) **499**, 419 (2013).
[2] R. Xiang *et al.*, Science **367**, 537 (2020).
[3] S. A. Claridge, A. Castleman, S. N. Khanna, C. B. Murray, and P. S. Weiss, ACS Nano **3**, 244 (2009).
[4] R. J. Nelmes, J. S. Loveday, D. R. Allan, J. M. Besson, G. Hamel, P. Grima, and S. Hull, Phys. Rev. B **47**, 7668 (1993).
[5] W. Krätschmer, L. D. Lamb, K. Fostiropoulos, and D. R. Huffman, Nature (London) **347**, 354 (1990).
[6] H. W. Kroto, J. R. Heath, S. C. O'Brien, R. F. Curl, and R. E. Smalley, Nature (London) **318**, 162 (1985).
[7] R. E. Marsh and D. P. Shoemaker, Acta Crystallogr. **6**, 197 (1953).
[8] M. Tegze and J. Hafner, Phys. Rev. B **40**, 9841 (1989).

[9] J. J. Zhao, Q. Y. Du, S. Zhou, and V. Kumar, Chem. Rev. **120**, 9021 (2020).
[10] C. Liu and Z.-M. Sun, Coord. Chem. Rev. **382**, 32 (2019).
[11] S. N. Khanna and P. Jena, Phys. Rev. Lett. **69**, 1664 (1992).
[12] H. Tsunoyama, H. Akatsuka, M. Shibuta, T. Iwasa, Y. Mizuhata, N. Tokitoh, and A. Nakajima, J. Phys. Chem. C **121**, 20507 (2017).
[13] M. Shibuta, T. Ohta, M. Nakaya, H. Tsunoyama, T. Eguchi, and A. Nakajima, J. Am. Chem. Soc. **137**, 14015 (2015).
[14] A. W. Castleman and S. N. Khanna, J. Phys. Chem. C **113**, 2664 (2009).
[15] P. Jena and Q. Sun, Chem. Rev. **118**, 5755 (2018).
[16] A. W. Castleman, J. Phys. Chem. Lett. **2**, 1062 (2011).
[17] Z. Luo and A. W. Castleman, Acc. Chem. Res. **47**, 2931 (2014).
[18] P. Jena, J. Phys. Chem. Lett. **4**, 1432 (2013).
[19] R. G. Parr and Z. Zhou, Acc. Chem. Res. **26**, 256 (1993).
[20] J. U. Reveles, S. Khanna, P. Roach, and A. Castleman, Proc. Natl. Acad. Sci. USA **103**, 18405 (2006).
[21] S. Zhou, Y. Y. Zhao, and J. J. Zhao, Chinese J. Struct. Chem. **39**, 1185 (2020).
[22] X. G. Gong and V. Kumar, Phys. Rev. Lett. **70**, 2078 (1993).
[23] S. N. Khanna, B. K. Rao, and P. Jena, Phys. Rev. Lett. **89**, 016803 (2002).
[24] M. B. Abreu, A. C. Reber, and S. N. Khanna, J. Phys. Chem. Lett. **5**, 3492 (2014).
[25] M. B. Abreu, A. C. Reber, and S. N. Khanna, J. Chem. Phys. **143**, 074310 (2015).
[26] H. Hiura, T. Miyazaki, and T. Kanayama, Phys. Rev. Lett. **86**, 1733 (2001).
[27] J. U. Reveles and S. N. Khanna, Phys. Rev. B **74**, 035435 (2006).
[28] K. Koyasu, J. Atobe, M. Akutsu, M. Mitsui, and A. Nakajima, J. Phys. Chem. A **111**, 42 (2007).
[29] V. Kumar and Y. Kawazoe, Phys. Rev. Lett. **87**, 045503 (2001).
[30] V. Kumar and Y. Kawazoe, Phys. Rev. Lett. **88**, 235504 (2002).
[31] V. Kumar and Y. Kawazoe, Phys. Rev. Lett. **91**, 199901(E) (2003).
[32] X. Wu, S. Zhou, X. Huang, M. Chen, R. Bruce King, and J. Zhao, J. Comput. Chem. **39**, 2268 (2018).
[33] M. Ohara, K. Koyasu, A. Nakajima, and K. Kaya, Chem. Phys. Lett. **371**, 490 (2003).
[34] K. Koyasu, M. Akutsu, M. Mitsui, and A. Nakajima, J. Am. Chem. Soc. **127**, 4998 (2005).
[35] J. Lau *et al.*, Phys. Rev. A **79**, 053201 (2009).
[36] S. Furuse, K. Koyasu, J. Atobe, and A. Nakajima, J. Chem. Phys. **129**, 064311 (2008).
[37] V. Kumar and Y. Kawazoe, Appl. Phys. Lett. **83**, 2677 (2003).
[38] U. Rohrmann and R. Schäfer, Phys. Rev. Lett. **111**, 133401 (2013).
[39] C. Rajesh and C. Majumder, J. Chem. Phys. **128**, 024308 (2008).
[40] X. Chen, K. Deng, C. Xiao, J. Chen, and D. E. Ellis, Comput. Theor. Chem. **971**, 73 (2011).
[41] P. Pyykkö and N. Runeberg, Angew. Chem. Int. Ed. **41**, 2174 (2002).
[42] X. Li, B. Kiran, J. Li, H. J. Zhai, and L. S. Wang, Angew. Chem. Int. Ed. **41**, 4786 (2002).
[43] Y. Gao, S. Bulusu, and X. C. Zeng, J. Am. Chem. Soc. **127**, 15680 (2005).
[44] D. Toprek and V. Koteski, Comput. Theor. Chem. **1081**, 9 (2016).
[45] T. Yu, Y. Gao, D. Xu, and Z. Wang, Nano. Res. **11**, 354 (2018).
[46] T. Iwasa and A. Nakajima, J. Phys. Chem. C **117**, 21551 (2013).
[47] Y. Yong, H. Cui, Q. Zhou, X. Su, Y. Kuang, and X. Li, J. Phys. Chem. Solids **127**, 68 (2019).
[48] S. Park, G. Kim, and Y.-K. Kwon, RSC Adv. **4**, 192 (2014).
[49] N. Okada, N. Uchida, and T. Kanayama, J. Appl. Phys. **121**, 225308 (2017).
[50] R. Robles and S. N. Khanna, Phys. Rev. B **80**, 115414 (2009).
[51] T. Iwasa and A. Nakajima, J. Phys. Chem. C **116**, 14071 (2012).
[52] F. Duque, A. Mañanes, L. M. Molina, M. J. López, and J. A. Alonso, Int. J. Quantum Chem. **86**, 226 (2002).
[53] G. Kresse and J. Furthmuller, Phys. Rev. B **54**, 11169 (1996).
[54] G. Kresse and D. Joubert, Phys. Rev. B **59**, 1758 (1999).
[55] J. P. Perdew, K. Burke, and M. Ernzerhof, Phys. Rev. Lett. **77**, 3865 (1996).
[56] S. Grimme, J. Antony, S. Ehrlich, and H. Krieg, J Chem. Phys. **132**, 154104 (2010).
[57] R. Krishnan, J. S. Binkley, R. Seeger, and J. A. Pople, J. Chem. Phys. **72**, 650 (1980).
[58] M. Dolg, U. Wedig, H. Stoll, and H. Preuss, J. Chem. Phys. **86**, 866 (1987).
[59] M. Frisch *et al.*, Gaussian Inc., Wallingford, CT (2016).
[60] S. L. Dudarev, G. A. Botton, S. Y. Savrasov, C. J. Humphreys, and A. P. Sutton, Phys. Rev. B **57**, 1505 (1998).
[61] Z. Hu and H. Metiu, J. Phys. Chem. C **115**, 5841 (2011).
[62] Q. Feng, J. Phys.: Condens. Matter **32**, 445603 (2020).
[63] See Supplemental Material at http://link.aps.org/supplemental/10.1103/PhysRevMaterials.5.066001 for geometric and electronic properties of cluster monomers and dimers, benchmark calculations of C_{60} solid, structures and band diagrams of 2D and 3D cluster assemblies, and elastic constant, *ab initio* molecular dynamics, and phonon spectra results of 2D and 3D Ti@Ge_{16} assemblies.
[64] S. Saito and A. Oshiyama, Phys. Rev. Lett. **66**, 2637 (1991).
[65] R. L. Whetten, *The MRS Late News Session-Buckyballs: New Material Made from Carbon Soot* (Materials Research Society, Pittsburgh, 1990).
[66] N. P. Kobelev, Y. M. Soifer, I. O. Bashkin, and A. P. Moravski, Nanostruct. Mater. **6**, 909 (1995).
[67] Q. Sun, Q. Wang, T. Briere, and Y. Kawazoe, J. Phys.: Condens. Matter **14**, 4503 (2002).
[68] M. Torres, E. Fernández, and L. Balbás, J. Phys. Chem. C **115**, 335 (2010).
[69] M.-X. Chen and X. H. Yan, J. Chem. Phys. **128**, 174305 (2008).
[70] C. L. Reis, J. L. Martins, and J. M. Pacheco, Phys. Rev. B **76**, 233406 (2007).
[71] C. L. Reis and J. M. Pacheco, J. Phys.: Condens. Matter **22**, 035501 (2009).
[72] C. Reis and J. Pacheco, Phys. Rev. B **82**, 155440 (2010).
[73] H. L. Schmider and A. D. Becke, J. Mol. Struc.:THEOCHEM **527**, 51 (2000).
[74] Z.-j. Wu, E.-j. Zhao, H.-p. Xiang, X.-f. Hao, X.-j. Liu, and J. Meng, Phys. Rev. B **76**, 054115 (2007).
[75] J.-L. Li *et al.*, Phys. Rev. Lett. **88**, 066101 (2002).

[76] M. Nakaya, T. Iwasa, H. Tsunoyama, T. Eguchi, and A. Nakajima, Nanoscale **6**, 14702 (2014).
[77] T. Ohta, M. Shibuta, H. Tsunoyama, T. Eguchi, and A. Nakajima, J. Phys. Chem. C **120**, 15265 (2016).
[78] M. Nakaya, T. Iwasa, H. Tsunoyama, T. Eguchi, and A. Nakajima, J. Phys. Chem. C **119**, 10962 (2015).
[79] H. Tsunoyama, M. Shibuta, M. Nakaya, T. Eguchi, and A. Nakajima, Acc. Chem. Res. **51**, 1735 (2018).
[80] X. Zhong *et al.*, Nano Lett. **18**, 1483 (2018).
[81] L. Wang *et al.*, Nature (London) **570**, 91 (2019).
[82] Y. Kubota, K. Watanabe, O. Tsuda, and T. Taniguchi, Science **317**, 932 (2007).
[83] C. Ataca, H. Şahin, and S. Ciraci, J. Phys. Chem. C **116**, 8983 (2012).
[84] X.-X. Zhang, Y. You, S. Y. F. Zhao, and T. F. Heinz, Phys. Rev. Lett. **115**, 257403 (2015).
[85] W. A. De Heer, Rev. Mod. Phys. **65**, 611 (1993).
[86] Z. He, K. He, A. W. Robertson, A. I. Kirkland, D. Kim, J. Ihm, E. Yoon, G.-D. Lee, and J. H. Warner, Nano Lett. **14**, 3766 (2014).
[87] B. Huang, H. Xiang, J. Yu, and S.-H. Wei, Phys. Rev. Lett. **108**, 206802 (2012).
[88] A. Hashmi and J. Hong, J. Phys. Chem. C **119**, 9198 (2015).
[89] R. C. Xiao, D. F. Shao, W. J. Lu, H. Y. Lv, J. Y. Li, and Y. P. Sun, Appl. Phys. Lett. **109**, 122604 (2016).
[90] B. Liu and K. Zhou, Prog. Mater Sci. **100**, 99 (2019).
[91] M. Imada, A. Fujimori, and Y. Tokura, Rev. Mod. Phys. **70**, 1039 (1998).
[92] E. N. Esenturk, J. Fettinger, and B. Eichhorn, J. Am. Chem. Soc. **128**, 9178 (2006).
[93] C. Rajesh, C. Majumder, M. G. R. Rajan, and S. K. Kulshreshtha, Phys. Rev. B **72**, 235411 (2005).
[94] B. K. Rao, S. N. Khanna, and P. Jena, Phys. Rev. B **62**, 4666 (2000).
[95] X. L. Zhu, X. C. Zeng, Y. A. Lei, and B. Pan, J. Chem. Phys. **120**, 8985 (2004).
[96] B. R. Goldsmith, J. Florian, J.-X. Liu, P. Gruene, J. T. Lyon, D. M. Rayner, A. Fielicke, M. Scheffler, and L. M. Ghiringhelli, Phys. Rev. Mater. **3**, 016002 (2019).
[97] S. Bulusu and X. C. Zeng, J. Chem. Phys. **125**, 154303 (2006).
[98] J. Wang, G. Wang, and J. Zhao, Phys. Rev. B **64**, 205411 (2001).
[99] D. Wu, Q. Du, X. Wu, R. Shi, L. Sai, X. Liang, X. Huang, and J. Zhao, J. Chem. Phys. **150**, 174304 (2019).
[100] S. Yoo and X. C. Zeng, Angew. Chem. **117**, 1515 (2005).
[101] X. Wu, L. Sai, S. Zhou, P. Zhou, M. Chen, M. Springborg, and J. Zhao, Phys. Chem. Chem. Phys. **22**, 12959 (2020).